The Journal of Undergraduate Research in Physics

CONTENTS

VOLUME 9, NUMBER 2

MAY, 1991

Published by the Physics Department of Guilford College
for
The American Institute of Physics and The Society of Physics Students

THE JOURNAL OF UNDERGRADUATE RESEARCH IN PHYSICS

This journal is devoted to research work done by undergraduate students in physics and its related fields. It is to be a vehicle for the exchange of ideas and information by undergraduate students. Information for students wishing to submit manuscripts for possible inclusion in the Journal follows.

ELIGIBILITY

The author must have performed all work reported in the paper as an undergraduate. The subject matter of the paper is open to any area of pure or applied physics or physics related field.

SPONSORSHIP

Each paper must be sponsored by a full-time faculty member of the department in which the research was done. A letter from the sponsor, certifying that the work was done by the author as an undergraduate and the the sponsor is willing to be acknowledged in the paper, must accompany the manuscript if it is to be considered for publication.

SUBMISSION

Two copies of the manuscript, the letter from the sponsor and a telephone number where the author can be reached should be sent to:

Dr. Rexford E. Adelberger, Editor
THE JOURNAL OF UNDERGRADUATE
RESEARCH IN PHYSICS
Physics Department
Guilford College
Greensboro, NC 27410

FORM

The manuscript should be typed, double spaced, on 8 1/2 x 11 inch sheets. Margins of about 1.5 inches should be left on the top, sides, and bottom of each page. Papers should be limited to fifteen pages of text in addition to an abstract (not to exceed 250 words) and appropriate drawings, pictures, and tables. Manuscripts may be submitted on a disk that can be read by a MacIntosh™. The files must be compatible with MacWrite™ or MicroSoft Word™. Illustrations should be in a MacDraw™ or MacPaint™ PICT format.

ILLUSTRATIONS

Line drawings should be made with black ink on plain white paper. Each figure or table must be on a separate sheet. Photographs must have a high gloss finish.

CAPTIONS

A brief caption should be provided for each illustration or table, but it should not be part of the figure. The captions should be listed together at the end of the manuscript

EQUATIONS

Equations should appear on separate lines, and may be written in black ink.

FOOTNOTES

Footnotes should be typed, double spaced and grouped together in sequence at the end of the manuscript.

SUBSCRIPTION INFORMATION

The Journal is published bianually, with issue one appearing in October and issue two in April of the next year. There are two issues per volume.

TYPE OF SUBSCRIBER	PRICE PER VOLUME
Individual	$US 5.00
Institution	$US 10.00

Foreign subscribers add $US 2.00 for surface postage, $US 10.00 for air freight.

To receive a subscription, send your name, address, and check made out to **The Journal of Undergraduate Research in Physics (JURP)** to the editorial office:

JURP
Physics Department
Guilford College
Greensboro, NC 27410

Back issues may be purchased by sending $US 15.00 per volume to the editorial office.

The *Journal of Undergraduate Research in Physics* is published by the Physics Department of Guilford College for the American Institute of Physics and the Society of Physics. **ISSN 0731-3764**

FABRICATION AND OPTICAL PROPERTIES OF POROUS SILICON *

J.R. Payne
Department of Physics
Sam Houston State University
Huntsville, TX 77341

ABSTRACT

During the past several years, considerable interest has been generated by the possible use of porous silicon in the fabrication of electronic devices. This paper discusses the process by which porous silicon can be fabricated and procedures for controlling pore size. Infrared absorption spectra are presented to show the time dependent oxide formation in the pores as well as the changes in the spectral region containing the crystal's phonon modes.

INTRODUCTION

The anodization of silicon to form porous silicon was first reported by Uhlir and Turner in the late 1950's [1,2]. In recent years, there have been several papers published on a material known as porous silicon (PS) [3-10]. This material has been investigated for use in electronic device technology, high quality mechanical filters and, at Sam Houston State University (SHSU) and the Texas Accelerator Center (TAC), for novel crystal accelerators.

In electronic device technology, porous silicon has been investigated to facilitate very-large scale integration (VLSI). In this capacity, the silicon substrate is anodized slightly to create a porous silicon layer of 20-50 μm. This PS layer has a reported average specific surface area of 200 m^2/cm^3 [3,4], which is $2x10^5$ times greater than that of a bulk wafer. Because of this large specific area the PS layer will oxidize very quickly in a laboratory atmosphere. At temperatures of 1000 C the rate of oxidation is 10 to 1000 times greater than that of bulk silicon [5,6].

The main advantage of having a PS layer on the substrate instead of epitaxing an insulating SiO_2 layer is that the Si-substrate epitaxed with SiO_2 is too sensitive to wafer bowing and device failure during construction and or operation. The epitaxed layer, SiO_2, has a different thermal expansion coefficient than that of the substrate. This causes the device to be too temperature sensitive by creating unwanted Schottky barriers and parasitic drain capacitances outside a narrow range of operating temperatures. In some instances, the device will physically break if the temperature stress becomes too great [3]. With a Si/substrate:PS/layer, these problems are no longer as formidable because the PS layer is single crystal silicon [7,8] and thus the expansion coefficients are the same.

Porous silicon may be used as a high quality mechanical filter. This requires that the PS layer be lifted off of the anodized substrate in one piece, thus becoming a PS membrane with thickness determined by the thickness of the anodized surface layer. A method for this removal has been perfected at Texas A&M University (TAMU) and has had some limited success here

---

Jim Payne graduated from Sam Houston State University (SHSU) in August 1989 with a BS in Physics He is currently a first year graduate student in the Graduate Physics Program at SHSU. He is the past SPS Associate Zone Councillor for Zone 10 and past SPS Associate Zone Councillor Representative. He did this work while a senior and currently is still involved with the Texas Accelerator Center on the crystal, X-ray accelerator project.

at SHSU. The problem with having a PS membrane filter is that, over time, the membrane will no longer allow the filtered gas to pass through due to oxidation of the pores [3].

Recently, at SHSU, a study of porous silicon has been initiated to see if it may be used as a material that will be compatible with current theories for solid state, crystal X-ray accelerator technologies proposed by Tajima and Cavengo[9]. The small pores would act as channels to allow X-ray acceleration of muons or heavier, positively charged particles to very high energies (Tajima and Cavengo[9] have proposed that the acceleration gradient would be 10 TeV/m). This theory relies upon the periodic structure of the crystal lattice for resonance and accelerating potential. Porous silicon appears to have the correct periodicity to fit the existing theoretical model.

THEORY

The formation of porous silicon layers on silicon wafers is an electro-chemical process of anodic oxidation in hydrofluoric (HF) acid.. In a concentrated HF solution (48%-52% by volume), the following reaction occurs at the surface of a substrate [3] :

$$Si + 2HF + (2-n)h \rightarrow SiF_2 + 2H + ne \quad (1)$$

where h represents a hole, e an electron, n<2 and is related to the conduction and valence band efficiencies.

The SiF_2 is an unstable substance that reacts with HF acid forming silicic acid (H_2SiF_6) and hydrogen gas (H_2) via the following reactions [3]:

$$SiF_2 + 2HF \rightarrow SiF_4 + H_2 \quad (2)$$

$$SiF_4 + 2HF \rightarrow H_2SiF_6 \quad (3)$$

A porous layer is formed on the surface of the substrate during dissolution. Because of the needed holes (Equation 1), heavily doped p-type silicon works best since the majority carriers are holes. Anodic dissolution can occur with n-type silicon, but since the majority carriers are electrons, holes must be introduced. This may be done by illuminating the surface with high intensity light of wavelength less than 1200 nm. At these wavelengths electron-hole pairs will be produced in the substrate [3].

The dissolution of silicon in HF acid is a tetravalent dissolution and occurs both laterally and perpendicularly [3]. Under the presence of an electric field, a divalent, perpendicular, porous dissolution can occur, but only up to certain current densities [3]. Once a critical current density is exceeded, electro-polishing occurs and the dissolution is tetravalent. This critical current density depends upon the impurity doping concentration of the silicon.

While the porous silicon is forming, its thickness and pore diameter are functions of the current density and anodizing time. The current density above all others is the factor that controls the pore diameter.

PROCEDURE

Two designs of anodizing cells were used in the investigation, both made of polyvinyl chloride (PVC) parts that tested HF acid resistant {see Figures 1&2}. Both designs contain a vertically mounted silicon wafer that separates the cell into two chambers filled with electrolyte. This design allows for a more uniform ohmic contact

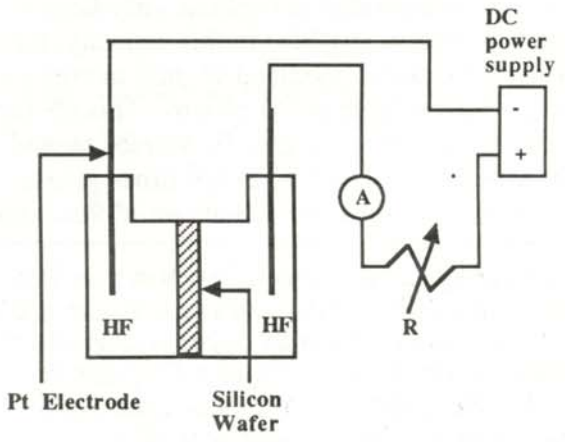

Figure 1
Design number 1 of the anodizing cell. This is the small cell. The circuit used to provide power is shown

with the electrolyte and facilitates easy removal of the H_2 gas bubbles that form during the reaction at the silicon-electrolyte interface. Both designs use platinum (Pt) electrodes that were fashioned from Pt wire and soldered to 26 gauge aluminum wire. A variable dc-power source was used to supply current (Lab Volt - Model 73P). A 200 kW resistor was connected in series to provide a more stable current . The first design, shown in Figure 1, was limited to small samples of cross-sectional areas of 1 cm^2 and thickness of 2 μm. The second design, shown in Figure 2 was more useful because it was adaptable and could accept various wafer sizes from 0.25-2 inches in diameter with thickness up to 1.5 inches.

The silicon wafers used for analysis were p-type, containing a wide range (10^{14}-10^{18} B/cm^3) of doping concentrations [15]. The wafers were highly polished on one side and lightly polished on the other side. No detailed characteristics of the samples, such as crystal plane orientation, resistivity or exact doping concentrations were available. One sample, however, was (1,1,0) oriented. It was heavy p-type with boron concentration of 10^{17}-10^{18} B/cm^3 and was 0.3 mm thick [11]. All other wafers were 0.5 mm thick.

Before anodization, the wafers were given a 30 sec dip in a dilute etch solution of HNO_3, HF, and glacial acetic acids in a volume ratio of 5:3:3. The wafers were then rinsed with distilled water and cleaned with acetone. If the first cell design was used, the wafer was placed between to rubber gaskets and the two chambers of the cell were tightened around the wafer until a water tight seal was formed. If the second cell design was used, the sample was first waxed onto the adaptable mount with a wax used to hold semiconductor boules for cutting and polishing. This wafer-waxed-to-mount seal was then tested for water tightness with distilled water. Upon a successful test the mount was inserted between the two chambers which were then tightened until a water tight seal was formed.

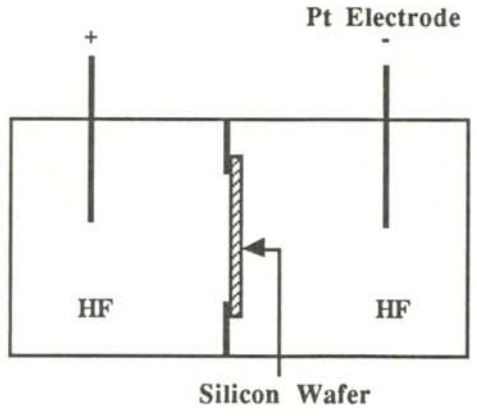

Figure 2
Design number 2 of the large anodizing cell

After the sample was mounted in either cell, a solution of 70% volume of HF and 30% volume ethanol was added to each of the two chambers. The ethanol provides for smoother electropolishing [10,3]. The power supply was adjusted so a current density of approximately 80 mA/cm^2 was maintained. This current density has been reported to be the ideal current density to form pores with a mean diameter of 20 Å in a heavy doped, p-type wafer [3].

When the current in the cell flows cathode (positive) to anode (negative), across the electrolyte solution, the anodization and subsequent pore formation occurs on the wafer surface that faces the anode. In this investigation, the polished side of the wafer's surface faced the anode. Immediately upon application of current to the circuit, H_2 gas bubbles boil away from both Pt electrodes and from the wafer surface being anodized. Little or no H_2 gas bubbles appear on the other wafer surface. The wafers were anodized for times ranging from 20 min to 2 hours.

After completion of anodization, the samples were cleaned again by the same method used in their preparation, but with only a 10 sec. dip in the etch solution. The newly anodized wafers were then placed under vacuum (10^{-3} torr) to remove any remaining electrolyte, or placed in hot box at 50 C overnight to help dry out the sample and speed up any oxidation wanted.

Figure 3
Transmission Electron Microscope photograph of the fractured surface of the 100 mm PS film. Along the surface, along the slant, a system of pores can be seen.

DISCUSSION OF RESULTS

The wafers underwent visually discernible physical changes during the anodization process. The polished surfaces that were exposed to anodization were discolored compared to the rest of their polished surface. They appeared light to dark blue-gray in fluorescent light. With some of the wafers, this discoloration was not blue-gray, but golden brown.

The sample with known orientation had already been anodized and contained a loose removable, 100 μm thick PS film which had a mean pore diameter of 20 Å [3]. This pore size was determined by the Brunhauer-Emmett-Teller method (BET) of gas absorption [12].

The samples were investigated by scanning electron microscopy (SEM), transmission electron microscopy (TEM), and Fourier transform infrared spectroscopy (FTIR). Unfortunately, the SEM work was too inconclusive to report here.

Because of its small size, the 100 μm sample was the only sample investigated by TEM [16]. Here again the results are not that conclusive. Figure 3 is a TEM photograph of the 100 μm thick PS sample at a magnification of 3 x 10^4. This shows a fractured surface of the porous material. Along the diagonal of the photograph (represented by arrows) a system of pores can be seen. The pores are represented by the dark spots on the white background, and are created by channeled electrons.

The FTIR data were taken with a Bomem DA3.01 Fourier transform spectrophotometer fitted with a potassium-bromide (KBr) beam-splitter and mercury-cadmium-telluride (MCT) detector. The typical absorbance spectrum at room temperature for a p-type single crystal of silicon appears in Figure 4. Closer examination in expanded scale of the expected phonon spectrum for this material is shown in Figure 5. These spectra were used as references for the anodized, porous samples.

The phonon spectrum of a slightly anodized (10 min at 20 mA/cm^2), p-type silicon substrate, 2 mm thick is shown in Figure 6. A comparison to Figure 4 reveals new features in the spectrum at the spectral regions near 2100 and 2900 cm^{-1}. For wavelengths larger than 1800 cm^{-1}, the expected silicon phonon spectrum is completely covered by a multitude of absorption peaks. These new features are the vibrational modes of silicon-monohydride (Si-H) and silicon dioxide (SiO_2) [13]. The spectrum for the 100 μm oriented film which contains average pore diameters of 20 Å is shown in Figure 7.

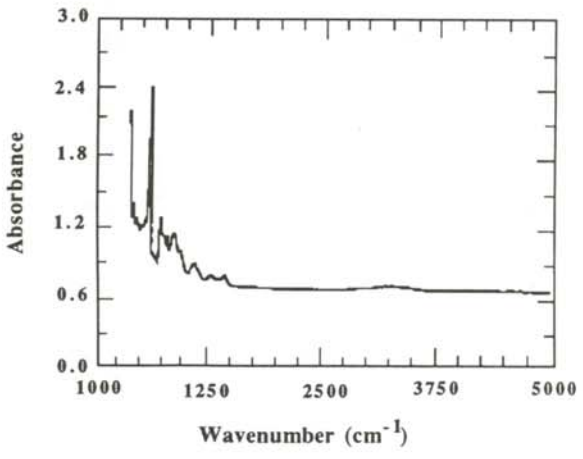

Figure 4
Typical absorbance spectrum at room temperature for a single crystal of p-type silicon.

There are similarities between the 100 μm PS-film and the thick, slightly anodized sample in the spectral regions near 2100 and 2900 cm^{-1}. These peaks are again attributed to complexes such as SiO_2 and Si-H which have formed in the pores. These complexes continue to form for an extended period of time after anodization. The absorption peaks as a function of time in the 100 μm PS-film are shown in Figure 8.

In conclusion, we have seen that the anodization of silicon to form PS physically changes the appearance of the surface to the unaided eye. Porous silicon contains a network of pores whose diameters can be controlled by current density, dopant concentration, and HF concentration. This anodization does not destroy the crystalline structure of the silicon, but creates two new features in the phonon spectrum (Si-H and SiO_2). The concentration of one of complexes, SiO_2, increases with time in an ambient atmosphere.

Currently, there are plans to perform proton channeling experiments on the porous films to measure the straightness of the pores.A study is planned of reactions of the PS layers in variously controlled atmospheres, and of annealing effects at different temperatures within these atmospheres.

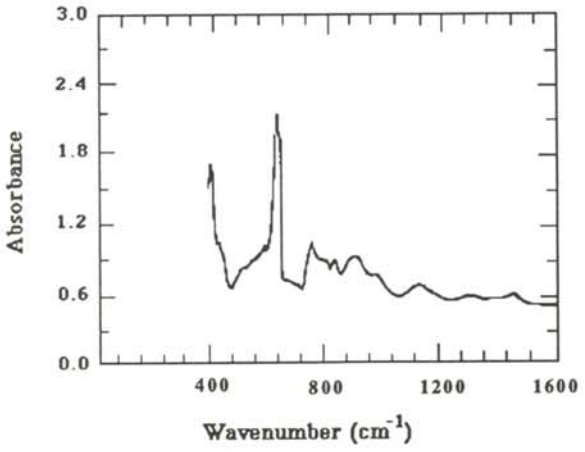

Figure 5
Expanded scale of the expected phonon spectrum at room temperature for a single crystal of p-type silicon.

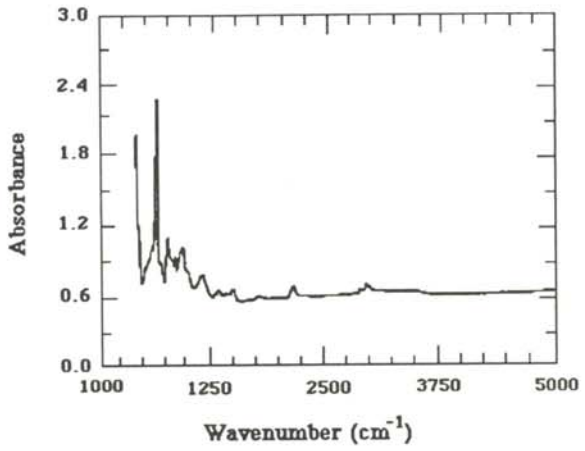

Figure 6
The phonon spectrum of slightly anodized p-type silicon.

ACKNOWLEDGMENTS

Funding for this project was provided by TAC and the Houston Advanced Research Center (HARC) both at The Woodlands, TX. The author would like to thank Dr. Russ Huson, Director of TAC (for allowing me to take part in this project), Dr. Barry Newberger and Dr. Toshi Tajima, Fusion Studies Group, University of Texas, Austin (for useful correspondence regarding the crystal X-ray accelerator concept), Dr. Terrell Hoage, Director of Electron Microscopy Lab, SHSU (for his time, assistance, and useful suggestions during the electron microscopy work), and Dr. Bill Covington, Chair of Physics, SHSU for reviewing and editing this manuscript.

REFERENCES

* Supported by the Texas Accelerator Center, Houston Advanced Research Center, and Sam Houston State University

1. A. Uhlir, Jr., Bell System Technical Journal 35, 333-347, 1956.

2. Dennis R. Turner, Journal of the Electrochemical Society 105, 402-408, 1958.

3. W.K. Yue, thesis, unpublished, TAMU, 1988.

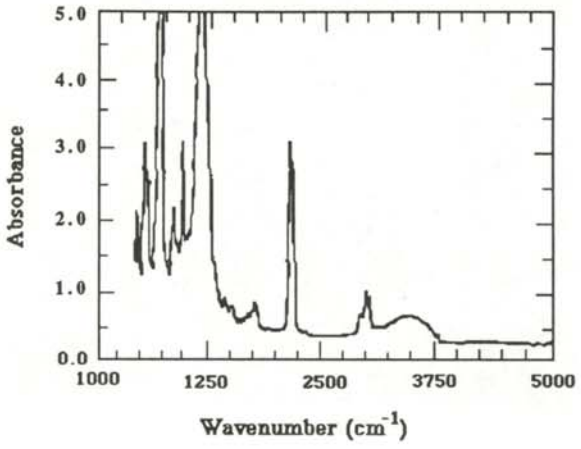

Figure 7
Phonon spectrum for the 100 μm PS film.

4. G. Bomchil, R. Herino, K. Barla, and J.C. Pfister, Journal of the Electrochemical Society 130, 1611-1614, 1983.

5. Kazou Imai and Hideyuki Unno, IEEE Transition on Electronic Devices ED-31, 297-302, 1984.

6. Hiroshi Takai and Tadatsugu Itoh, Journal of Electronic Materials, 12, 973-981, 1983.

7. Yoshinobu Arita and Yoshio Sunohara, Journal of the Electrochemical Society, 124, 285-295, 1977.

8. M.I.J Beale, N.G. Chew, M.J. Uren, A.G. Cullis, and J.D. Benjamin, Applied Physics Letters, 46, 86-88, 1985.

9. T. Tajima and M. Cavengo, Physical Review Letters, 59 , 1440-1443, 1987.

10. R. Herino, A Perio, K. Barla, and G. Bomchil, Materials Letters, 2, 519-523, 1984.

11. Wing Yue, private conversation.

12. Stephen Brunhauer, P.H. Emmett, and Edward Teller, Journal of Applied Physics, 60, 309-319, 1938.

13. J.W. Anderson, CRC Handbook of Spectroscopy Vol. 2, 11, 1974.

14. J.W. Anderson, CRC Handbook of Spectroscopy Vol. 2, 72, 1974.

15. The wafers were provided by Dr. Bill Covington of the SHSU Physics Department.

16. This photograph was taken with the transmission electron microscope in the Electron Microscopy Lab in the Biology Department of SHSU.

FACULTY SPONSOR

Dr. Bill Covington
Department of Physics
Sam Houston State University
Huntsville, TX 77341
409-294-1601

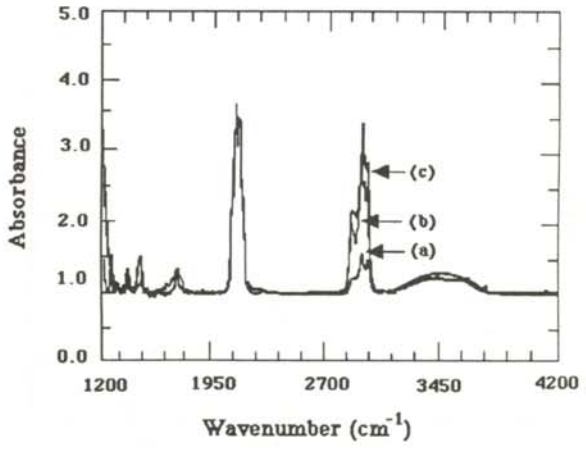

Figure 8
Phonon spectrum of 100 μm PS film as a function of time: a) one day after anodizing, b) two weeks after anodizing and c) one month after anodizing.

'MAXWELL'S EQUATIONS' FOR GRAVITATION

Amanda J. McDonald
Department of Physics
Southern Nazarene University
Bethany, OK 73008

ABSTRACT

The 'gravomagnetic' field of a uniformly moving mass [1] is generalized to time-dependent situations. The result, though non-rigorous, is a set of 'Maxwell's equations' quite similar to those of electrodynamics.

1. H. Kolbenstvedt, Am. J. Phys. 56, 523-524, 1988

INTRODUCTION

In a recent article, Kolbenstvedt [1] derived an expression for the 'gravomagnetic' field produced by a uniformly moving mass at the limit of small velocities. Except for a factor of 2, the result is identical to the prediction of linearized general relativity.[2] The appeal of this approach is its simplicity, making it available to undergraduates familiar with electrodynamics and special relativity. This paper is an expansion of the derivation to include time-dependent 'gravoelectric' and 'gravomagnetic' fields and the accompanying 'Maxwell's equations' for the 'gravomagnetic' system.

Besides the practical value of being able to estimate 'gravodynamic' fields by borrowing solutions from electrodynamics, our derivation of 'Maxwell's equations' for the 'gravodynamic' field, though non-rigorous, is a useful exercise in using known or assumed constraints to suggest the form of the field equations. In this way, one can build intuition of what to expect qualitatively from the result of a rigorous derivation.

Joy was a senior at Southern Nazarene University in Bethany, OK when this research was completed. She spent a summer studying atomic physics in Los Alamos, New Mexico. She is now working as an insurance actuary.

The 'Gravomagnetic Field'

This section is a review of Kolbenstvedt's [1] derivation of the gravomagnetic field. Consider a particle of mass M moving with constant velocity V along the positive x axis of the laboratory frame, where $V << 1$ (in units where $c = 1$). M is the source of the gravitational field:

$$\mathbf{g} = -\nabla \phi \tag{1}$$

As seen in M's rest frame, the motion of a test particle of mass m is given by:

$$\delta \int (-m\, ds) = 0$$

$$-m\, ds = -m \left[(1 + 2\phi_o)^2\, dt_o^2 - dr_o^2 \right]^{1/2} \tag{2}$$

where ϕ_o is the gravitational potential:

$$\phi_o = - GM/r_o \ . \qquad (3)$$

The only input from general relativity has been to insert into the metric of flat space-time the Newtonian limit of the time-time component of the metric tensor [3],

$$g_{oo} \approx - (1 + 2 \phi), \qquad (3)$$

The Lorentz transformation to the laboratory frame to the first order in V is:

$$\begin{aligned} x_o &\approx x - Vt \\ y_o &= y \\ z_o &= z \\ t_o &\approx t - Vx \ . \end{aligned} \qquad (4)$$

If ϕ is assumed to be approximately invariant, the motion of the test particle in the laboratory is determined by :

$$\delta \int L \, dt = 0 \quad , \qquad (5)$$

where

$$L \, dt = -m \, [\{1 + 2\phi(\mathbf{r},t)\} \, (dt - Vdx)^2 - (dx - Vdt)^2 - dy^2 - dz^2 \,]^{1/2} \ . \qquad (6)$$

To the first order in V, equation 6 yields

$$L = -m \, [\, 1 - v^2 + 2\phi - 4 \, \phi \, \mathbf{V}\cdot\mathbf{v}] \, ^{1/2} \ , \qquad (7)$$

where $\mathbf{v} = d\mathbf{r}/dt$ is the velocity of the test particle in the laborataory frame.

Consider the case where the source particle moves very slowly compared to the test particle and where the test particle's kinetic and potential energies are of like order of magnitude, ie. $V \ll 1$, $v \ll 1$ and $\phi \approx v^2 \ll 1$. Equation 7 then reduces to:

$$L \approx 1/2 \, m \, v^2 - m\phi + 2 \, m \, \phi \, \mathbf{V}\cdot\mathbf{v} \ . \qquad (8)$$

The Lagrangian of a non-relativistic particle of mass m and charge q moving in an externally applied electromagnetic field with scalar potential U and vector potential **A** is:

$$L_{em} = 1/2 \, m \, v^2 - qU + q \, \mathbf{A}\cdot\mathbf{v}. \qquad (9)$$

Comparing Equation 8 to Equation 9 produces the familiar analogy that $m\phi$ corresponds to qU and, in addition, the less familiar correspondence where $2m\phi\mathbf{V}$ is the gravitational analog to $q\mathbf{A}$.

In this context, the gravitational field **g** produced by a point source is now the 'gravoelectric field'

$$\mathbf{g} = - \nabla\phi = (GM/r^3) \, (-\mathbf{r}) \qquad (10)$$

(neglecting retardation effects). The analogy also suggests the existence of a 'gravomagnetic field' **b** produced by a moving mass:

$$\mathbf{b} = \nabla \times (2\phi\mathbf{V}) = 2\mathbf{V} \times (-\nabla\phi) = 2\mathbf{V} \times \mathbf{g}. \qquad (11)$$

The equation of motion of the test particle becomes:

$$\mathbf{g} + (\mathbf{v} \times \mathbf{b}) = d\mathbf{v}/dt \ . \qquad (12)$$

'MAXWELL'S EQUATIONS' FOR g AND b

For a continuous mass distribution,

$$\phi(\mathbf{r}) = - G \int \rho(\mathbf{r}') / R \ d^3\mathbf{r}' \qquad (13)$$

$$\mathbf{g}(\mathbf{r}) = - G \int \rho(\mathbf{r}') \, \mathbf{R}/R^3 \ d^3\mathbf{r}' \ , \qquad (14)$$

where $\rho(\mathbf{r}')$ is the mass density and $\mathbf{R} = \mathbf{r} - \mathbf{r}'$ is the vector from the source point $\mathbf{r}'$ to the field point $\mathbf{r}$. Equation 14 is the 'Coulomb's law' of the gravoelectric field, ie., Newton's law of gravitation.

Since $\mathbf{g} = - \nabla\phi$,

$$\nabla \times \mathbf{g} = \mathbf{0} \qquad (15)$$

and

$$\begin{aligned} \nabla \cdot \mathbf{g} = - \nabla^2\phi &= G \int \rho(\mathbf{r}') \, \nabla^2(1/R) \, d^3\mathbf{r}' \\ &= - 4 \pi G \int \rho(\mathbf{r}') \, \delta^3(\mathbf{r} - \mathbf{r}') \ d^3\mathbf{r}' \qquad (16) \\ &= - 4 \pi G \, \rho(\mathbf{r}) \ . \end{aligned}$$

where $\delta^3(\mathbf{r} - \mathbf{r}')$ is the delta function and the gradient, ∇, operates on the field point coordinates.

The 'gravomagnetic field' for an extended source of current can be written as:

$$\begin{aligned} \mathbf{b}(\mathbf{r}) &= 2 \int \mathbf{V}(\mathbf{r}') \times [-G \rho(\mathbf{r}') \mathbf{R}/R^3] \, d^3\mathbf{r}' \\ &= -2G \int \mathbf{j}(\mathbf{r}') \times \mathbf{R}/R^3 \, d^3\mathbf{r}' , \end{aligned} \tag{17}$$

where $\mathbf{j} = \rho\mathbf{V}$ is the source current density. Equation 17 is the 'Biot-Savart' law of the gravomagnetic field. Like their electromagnetic analogs, the 'Coulomb' and 'Biot-Savart' laws are the whole story of **g** and **b** only for static mass densities and steady current densities.

Equation 17 can be rewritten as:

$$\mathbf{b}(\mathbf{r}) = -2 G \nabla \times \int \mathbf{j}(\mathbf{r}')/R \, d^3\mathbf{r}' . \tag{18}$$

It follows then that:

$$\nabla \cdot \mathbf{b} = 0 . \tag{19}$$

Equation 17 also suggests writing the vector potential **a** (where $\mathbf{b} = \nabla \times \mathbf{a}$) as:

$$\mathbf{a} = -2 G \int \mathbf{j}(\mathbf{r}')/R \, d^3\mathbf{r}' . \tag{20}$$

To evaluate $\nabla \times \mathbf{b}$, we use the identity:

$$\nabla \times \mathbf{b} = \nabla \times (\nabla \times \mathbf{a}) = \nabla (\nabla \cdot \mathbf{a}) - \nabla^2 \mathbf{a} . \tag{21}$$

The $\nabla (\nabla \cdot \mathbf{a})$ term may be disposed of either by the proof of the Helmholtz theorem [4] or by an appeal to gauge invariance (choose a gauge $\nabla \cdot \mathbf{a}$ = spatial constant). This leaves:

$$\begin{aligned} \nabla \times \mathbf{b}(\mathbf{r}) &= 2 G \nabla^2 \int \mathbf{j}(\mathbf{r}')/R \, d^3\mathbf{r}' \\ &= 2 G \int \mathbf{j}(\mathbf{r}') \nabla^2 (1/R) \, d^3\mathbf{r}' \\ &= -8 \pi G \mathbf{j}(\mathbf{r}). \end{aligned} \tag{22}$$

The time-independent 'Maxwell's equations' for the 'gravoelectric' and 'gravomagnetic' fields are:

$$\begin{aligned} \nabla \cdot \mathbf{g} &= -4 \pi G \rho \\ \nabla \cdot \mathbf{b} &= 0 \\ \nabla \times \mathbf{g} &= \mathbf{0} \\ \nabla \times \mathbf{b} &= -8 \pi G \mathbf{j} . \end{aligned} \tag{23}$$

Now, we allow the sources to become time-dependent. Let us assume local conservation of mass:

$$\nabla \cdot \mathbf{j} = -\partial\rho/\partial t . \tag{24}$$

This is not consistent with Ampere's law for **b** (Equation 21) which requires the divergence of **j** to vanish identically. However, from Gauss' law for **g** (Equation 16) we have:

$$\partial\rho/\partial t = -1/(4\pi G) \nabla \cdot (\partial \mathbf{g}/\partial t), \tag{25}$$

which suggests that the time-dependent version of Ampere's law should be:

$$\begin{aligned} \nabla \times \mathbf{b} &= -8 \pi G[\mathbf{j} + 1/(4\pi G) (\partial \mathbf{g}/\partial t)] \\ &= -8 \pi G \mathbf{j} + 2 \partial \mathbf{g}/\partial t . \end{aligned} \tag{26}$$

Let us now consider how Equation 15 should be modified when time-dependent fields may exist. We propose the modification:

$$\nabla \times \mathbf{g} = \mathbf{s} , \tag{27}$$

where **s** must vanish when the fields are static. In the 'derivation' of the 'gravomagnetic field', retardation effects were assumed to be negligible. Now, they must be taken into account. Inspired by electrodynamics, we assume that changes in the 'gravoelectric' or 'gravomagnetic' fields propagate as waves moving at the speed of light (indeed, this is predicted by general relativity [5]). This suggests writing a wave equation for **g** of the form:

$$\nabla^2 \mathbf{g} - \partial^2 \mathbf{g}/\partial t^2 = 0 \tag{28}$$

in source-free regions. Making use of the iden-

tity of Equation 21, Equation 27 can be written as:

$$\nabla \times \mathbf{s} = \nabla \times (\nabla \times \mathbf{g}) = \nabla (\nabla \cdot \mathbf{g}) - \nabla^2 \mathbf{g}. \quad (29)$$

In source-free regions, $\nabla \cdot \mathbf{g} = 0$, so Equation 29 becomes:

$$\nabla^2 \mathbf{g} + \nabla \times \mathbf{s} = 0 , \quad (30)$$

yielding

$$\nabla \times \mathbf{s} = - \partial^2 \mathbf{g}/\partial t^2 . \quad (31)$$

Taking the partial time derivative of Equation 26 results in:

$$\partial^2 \mathbf{g}/\partial t^2 = 1/2 [\nabla \times (\partial \mathbf{b}/\partial t)] . \quad (32)$$

Comparing Equation 31 to Equation 32, we deduce that:

$$\mathbf{s} = -1/2 \, \partial \mathbf{b}/\partial t . \quad (33)$$

The modified Equation 15 then becomes 'Faraday's law':

$$\nabla \times \mathbf{g} = -1/2 \, \partial \mathbf{b}/\partial t . \quad (34)$$

Defining $\mathbf{b}' = 1/2 \, \mathbf{b}$, the 'Maxwell's equations' for the 'gravodynamic fields' $\mathbf{g}$ and $\mathbf{b}'$ are:

$$\begin{aligned} \nabla \cdot \mathbf{g} &= - 4 \pi G \rho \\ \nabla \cdot \mathbf{b}' &= 0 \\ \nabla \times \mathbf{g} &= -\partial \mathbf{b}'/\partial t \\ \nabla \times \mathbf{b}' &= - 4 \pi G \mathbf{j} + \partial \mathbf{g}/\partial t . \end{aligned} \quad (35)$$

The derivation of these results and the application of the 'gravomagnetic Maxwell's equations' are useful exercises. The correct procedure would be to investigate the linearized field equations of general relativity. But with the results above, known solutions to electrodynamics problems could be applied to gravitational systems in motion. This might help build intuition about anticipated qualitative features of the solutions.

REFERENCES

1. H. Kilbenstvedt, Am.J.Phys. 56, 523-524, 1988.

2. S. Weinberg, Gravitation and Cosmology: Principles and Applications of the General Theory of Relativity, Wiley, New York, 1972, Chapter 9. For instance, Equation 20 in this paper is Weinberg's equation 9.1.62 to within a factor of 2.

3. Ibid., Chapter 3.

4. W.K.H. Panofsky and M. Phillips, Classical Electricity and Magnetism, Addison-Wesley, Reading, MA, 1962, Chapter 1.

5. S. Weinberg, op. cit., Chapter 10.

FACULTY SPONSOR

Dr. Dwight E. Neuenschwander
Department of Physics
Southern Nazarene University
Bethany, OK 73008

FILTERING PROPERTIES OF A MULTIPLE FABRY-PEROT INTERFEROMETER

Thomas Greco *
Department of Physics
Central Michigan University
Mt. Pleasant, MI 48859

ABSTRACT

The standard textbook discussion of the Fabry-Perot interferometer is extended to include the evaluation of the phase-shift in addition to intensity of the transmitted wave. The results are used to derive the properties of multiple etalon combinations. Analytical solutions are illustrated by computer generated diagrams.

INTRODUCTION

Fabry-Perot interferometry is one of the more important techniques of high resolution spectroscopy, so thorough understanding of the principles of operation of a Fabry-Perot interferometer (F-P) is important. In addition, many properties of laser light (eg. its modal structure) can be obtained by analysis of the interference phenomena that arise in the passive mirror cavity of the F-P.

The derivation of the transmission function for a single F-P presents an interesting, although not extremely complicated, example of a practical application of the wave superposition principle. For this reason, it appears in most books and courses dealing with wave optics. [1]. However, the discussions of the transmission properties of multiple F-P's have been somewhat neglected.

There are two main multiple F-P systems : 1) combinations of F-P's in series, and 2) one F-P within another's cavity. The latter system should be helpful in understanding the mode selection procedures in different kinds of lasers by use of intracavity etalons. In this paper, these two systems are modeled analytically and the results illustrated by computer generated graphs.

F-P TRANSMISSION FUNCTION

A F-P consists of two reflective, flat, parallel surfaces a distance d apart. Incident light is partially reflected and partially transmitted by each surface, setting up multiple reflections between the two surfaces as shown in Figure 1. Constructive interference among transmitted beams takes place when different contributions are delayed by $m\lambda$, where m is an integer and λ is the wavelength of the incident light. When this condition is satisfied, transmission will be 100 percent.

Tom graduated from Central Michigan University in 1990 and is now a graduate student at Old Dominion University. His goal is to earn a Ph.D. in physics and then continue doing research in a university setting.

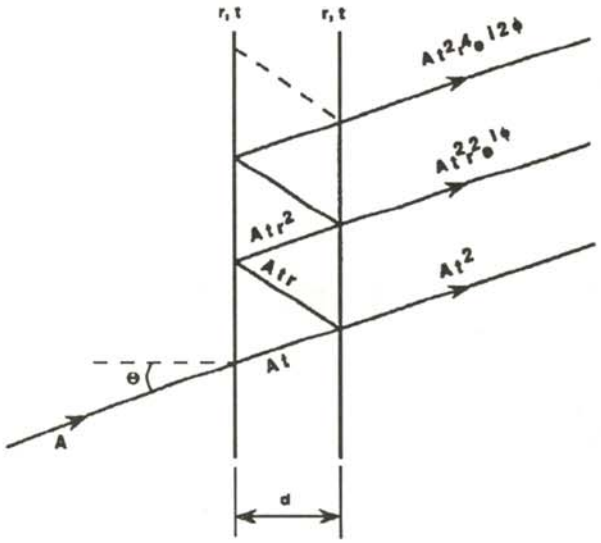

Figure 1
A simple Fabry-Perot interferometer showing multiply transmitted and reflected beams.

The transmission function can be calculated assuming the two surfaces are flawless, perfectly parallel, non-absorbing mirrors and that the incident light is a monochromatic plane wave. If the mirrors have amplitude transmission coefficient τ and reflection coefficient r and are separated by a distance d, the transmitted amplitude is [2]:

$$A_T = A \frac{T}{1 - R\, e^{i\phi}} \qquad (1)$$

where $T = \tau^2$ is the intensity transmission coefficient, $R = r^2$ is the intensity reflection coefficient and $\phi = 2kd\cos\theta$ where k is $2\pi/\lambda$ and θ is the angle the light strikes the F-P. The intensity of the transmitted beam is the square of the amplitude of the transmitted wave:

$$I_T = A_T^* A_T = \frac{A^2 T^2}{(1-R)^2} \frac{1}{1 + F\sin^2(\phi/2)} \qquad (2)$$

where $F = 4R/(1-R)^2$. Since the system is assumed to be absorptionless, T+R=1, the relative fractional transmission can be written as:

$$\frac{I_T}{I_o} = \frac{1}{1 + F\sin^2(\phi/2)} \qquad (3)$$

Figure 2 shows the result graphically. As the reflectivity increases, the transmission peaks become very narrow and the transmission drops almost to zero in between them. For this reason, F-P's with high reflectivity (80% - 95%) can be used as narrow tunable filters. By varying the mirror separation, one can scan spectra with very narrow bandwidths.

Phase of the Emerging Wave

Placing a F-P interferometer in a light beam not only affects the amplitude of the emerging beam, but also produces a phase shift between the incident and transmitted radiation. This phase shift can be calculated by writing Equation 1 in (x + iy) form using the relationship:

$$\rho\, e^{i\phi} = \rho\, \{\cos\phi + i\sin\phi\}. \qquad (4)$$

The transmitted electric field becomes:

$$\frac{E_T}{E_o} = \frac{1 - R\cos\phi + i\,R\sin\phi}{(1 - R\cos\phi)^2 + R^2\sin^2\phi} \qquad (5)$$

Now, putting Equation 5 back into magnitude-phase form yields:

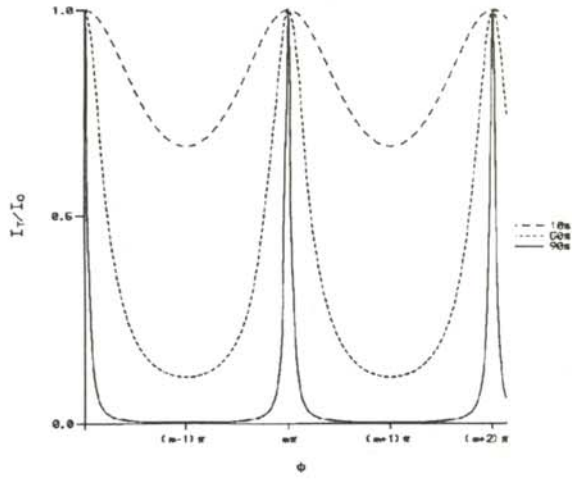

Figure 2
Plot of the fraction of transmitted light as a function of

$$E_T = \tau E_o e^{i\psi}$$

$$\psi = \tan^{-1}\left(\frac{R \sin\phi}{1 - R\cos\phi}\right) \qquad (6)$$

$$\tau = \{ (1 - R\cos\phi)^2 + R^2 \sin^2\phi \}^{-\frac{1}{2}}$$

Figure 3 is a plot of the phase phase shift between the transmitted and incident electric field as a function of the single contribution phase shift ϕ. The zero phase shift at points corresponding to maximum transmission is expected since here all contributions come in phase, There is also a zero phase shift at the minima where every other contribution is in exactly opposite phase. For high reflectivity, the phase change is very rapid around the maxima where there is interference among many phase shifted contributions of comparable magnitude. However, there is not much of a phase shift for low reflectivity due to the domination of the first contribution in the transmitted beam.

Double F-P Combinations

One way of constructing a F-P combination is by passing radiation through two separate F-P's in series. In most cases, this has no great practical advantage as a filter because the resolution

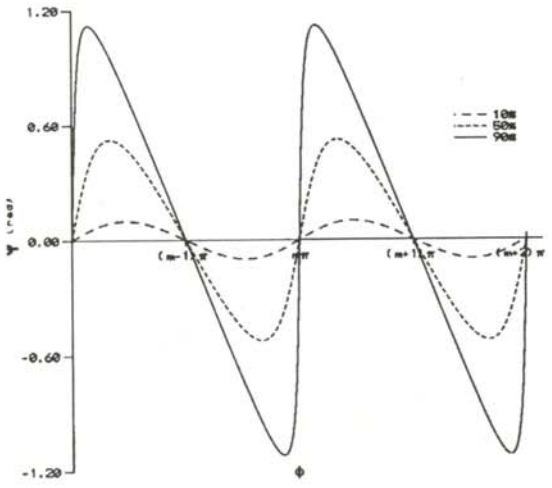

Figure 3
Net phase shift of the transmitted wave versus F-P round trip phase shift.

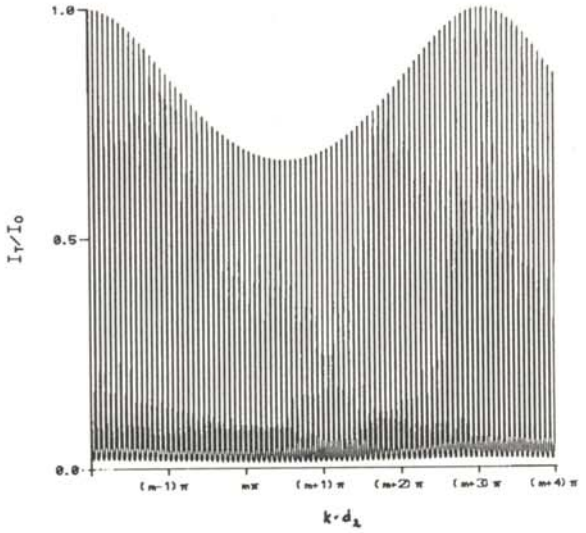

Figure 4
Transmitted intensity versus wave number of the incident light beam. The beam crosses two F-P's with mirrors of different reflectivities and separations ($R_1 = 10\%$, $R_2 = 90\%$, $d_1/d_2 = 15$).

will be limited to that of the F-P with the highest reflectivity. Never-the-less, it is demonstrative of the properties that F-P's possess.

Let the first F-P have a high reflectivity, a large mirror separation and be perpendicular to the incident beam. Its transmission peaks will be narrow and closely spaced in k. A phase shift $\phi_1 = 2kd_1$ is produced on each round trip through the interferometer. The final phase shift ψ_1 is found by substituting this value into Equation 6.

Assume the second F-P has a lower reflectivity and a smaller separation to give broad transmission peaks. In addition, tilt the second F-P at a small angle θ so as to include only those reflections occurring between mirrors belonging to the same F-P. The round trip phase shift of the second F-P is $\phi_2 = 2kd_2\cos\theta$. Again, Equation 6 can be used to find the final phase shift ψ_2. Since there are no interference effects between the two F-P's the transmission function of the series is just the product of the transmission functions for each individual F-P:

$$\frac{I_T}{I_o} = \frac{1}{1 + F_1 \sin^2(kd_1)} * \frac{1}{1 + F_2 \sin^2(kd_2)} \qquad (7)$$

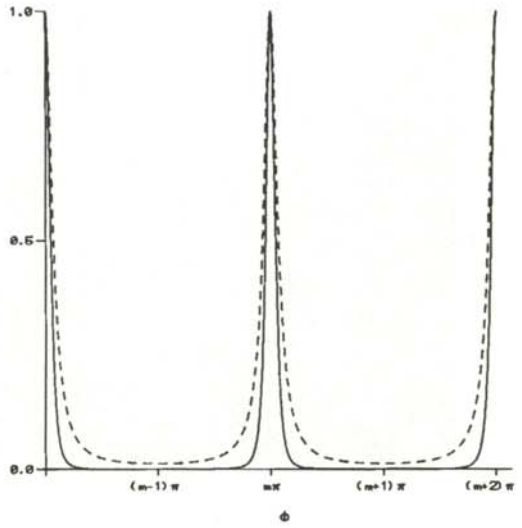

Figure 5
Transmitted intensity versus round trip phase shift for double pass configureation as compared with a single pass configuration. The dashed lines are the single pass results while the solid line represents the double pass.

and the net phase shift with respect to the unobstructed beam is:

$$\Psi = \Psi_1 + \Psi_2 \qquad (8)$$

Figure 4 shows the superposition of the individual transmission functions that occurs when the two F-P's described are placed in series.

An interesting configuration for a filter is made of a series of two highly reflective F-P's with identical parameters. In this case, the product of the transmission functions produces peaks which are narrower than those of the individual F-P, yet they still reach 100% at maximum transmission. In practice, instead of setting up two F-P's, it makes more sense to make a double pass through a single F-P by reflecting the transmitted beam back with a cube corner reflector. [3]

For a double pass configuration, the transmitted intensity is the square of the single F-P transmission function of Equation 3. Figure 5, a comparison of single and double passes through a filter, shows markedly narrower transmission peaks for the double pass filter. This is useful when trying to resolve a spectrum in which adjacent bands are very close together or when it is critical to have a high contrast.

F-P Within the Cavity of Another F-P

The final and perhaps most important consideration for multiple F-P's is for one etalon to be placed inside another's cavity as shown in Figure 6. Calculations of the transmission coefficient are simplified if the individual reflections and transmissions of the inner F-P are not considered but are dealt with as a single transmission function and total phase shift. This transmission function is applied to the individual beams moving through the outer F-P.

For the inner F-P, the field amplitude transmission coefficient $A_T/A = \tau\, e^{i\Psi 2}$, is obtained directly from Equation 6 with $\phi_2 = 2kd_2\cos\theta$. The most direct (n = 0) contribution crosses the first mirror of the outer F-P, passes through the intra-cavity F-P, and then crosses the second mirror of the outer F-P. If the amplitude of the input beam is A, this contribution will have amplitude

$$A_o = A\, t_1^2\, \tau\, e^{i\Psi 2}. \qquad (9)$$

Each consecutive contribution has to bounce two extra times off the external mirrors and go twice through the intra-cavity F-P. The additional travel results in a phase shift which is a combination of the phase shift produced by the distance travelled between the external mirrors (ψ_1) and the phase shift produced by the inner F-P alone (ψ_2). Therefore, each individual contribu-

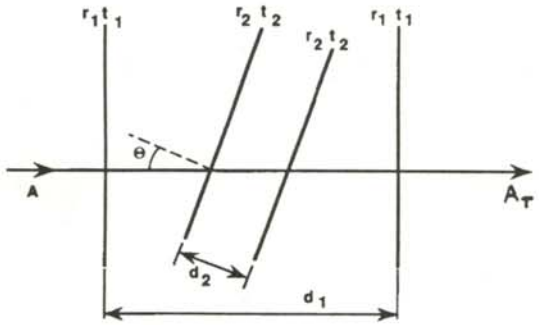

Figure 6
Tilted intracavity etalon as an additional filtering element.

tion to the field amplitude is:

$$A\, t_1^2\, \tau\, e^{i\psi 2}\, r_1^{2n}\, \tau^{2n}\, e^{i2n\psi 2}\, e^{in\psi 1}\,, \qquad (10)$$

where n is the number of bounces off the second mirror of the outside F-P. The amplitude of the transmitted wave can be expressed as a series of the individual contributions:

$$A_T = AT_1\tau e^{i\psi 2}\,[1 + R_1\tau^2 e^{i(\psi 1 + 2\psi 2)} + \{ R_1\tau^2 e^{i(\psi 1 + 2\psi 2)} \}^2 + \{R_1\tau^2 e^{i(\psi 1 + 2\psi 2)} \}^3 + ...] \qquad (11)$$

where $t_1^2 = T_1$ and $r_1^2 = R_1$. The sum of this geometric series is:

$$A_T = \frac{A\, T_1\, \tau\, e^{i\psi_2}}{1 - R_1\, \tau^2\, e^{i(\psi_1 + 2\psi_2)}}\,. \qquad (12)$$

The transmitted intensity is obtained by taking the square of the amplitude:

$$I_T = A_T^* A_T = \frac{A^2\, T_1^2\, \tau^2}{1 + R_1^2\, \tau^4 - R_1\tau^2\, [\, e^{i(\psi_1 + 2\psi_2)} + e^{-i(\psi_1 + 2\psi_2)}\,]}\,, \qquad (13)$$

Which can be written as:

$$\frac{I_T}{I_o} = \frac{T_1^2\, \tau^2}{(1 - R_1\, \tau^2)}\, \frac{1}{1 + F \sin^2\left(\frac{\psi_1}{2} + \psi_2\right)}\,, \qquad (14)$$

where $F = 4R_1\, \tau^2/[1 - R_1\, \tau^2]^2$

.

Figure 7 is a plot of this this transmission function. It shows that the intra-cavity etalon configuration can produce the narrowest transmission peaks as well as the broadest free spectral range. These features are important when trying to resolve a spectrum which consists of many lines within a range of wavelengths that is too broad for a traditional F-P.

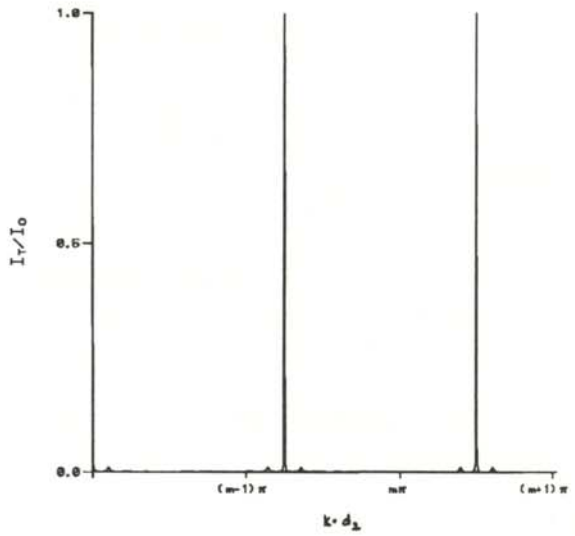

Figure 7
Iransmitted intensity versus incident beam wave number for intracavity etalon configuration. For the external F-P, $R_1 = 95\%$; for the intracavity etalon, $R_2 = 50\%$; and $d_1/d_2 = 10$

Although we are not aware of using intra-cavity combinations in practical spectral analysis, it may be worth trying out a few possibilities. The filtering power of the intra-cavity etalons has been utilized successfully in suppression of unwanted modes in laser emission. It may not seem as through an F-P with low reflectivity (such as seen in Figure 2) can still be very effective as a spectral filter, However, the calculations presented here show how intra-cavity placement improves filtering properties of etalons and may be used to construct F-P combinations for specific needs.

SUMMARY

We have shown that the full analysis of a F-P etalon must include its effects on the amplitude and the phase of a light beam. The phase shift is not of great importance when a single etalon is considered. However, it becomes very important in the operation of an intra-cavity etalon. This discussion shows the power of intra-cavity placement for a low finesse F-P. The formalism can be extended to multiple intra-cavity etalon combinations such as those used in a single mode selection of a tunable dye laser.

ACKNOWLEDGEMENTS

The author acknowledges with kindness the summer support provided by the Research Corporation.

REFERENCES

* Current Address of the author: Physics Department, Old Dominion University, Norfolk, VA 23529-0116.

1. R. Guenther, Modern Optics, Wiley and Sons, Inc., New York, 1990, pp.106-114.

2. E. Hecht, Optics, Addison Wesley Co., Reading, 1987, p. 366.

3. Fabry-Perots, Technical memo for Fabry-Perot Interferometry, Burleigh Instruments Inc., 1976.

4. P. Milonni and J. Eberly, Lasers, Wiley and Sons, Inc., new York, 1988, pp. 354-359.

FACULTY SPONSOR

Dr. Andy Sieradzan
Department of Physics
Central Michigan University
Mount Pleasant, MI 48859

GAS MONITOR CHAMBER FOR PARTICLE PHYSICS EXPERIMENTS *

Károly Banicz
Eötvös Lóránd University
Budapest, Hungary

ABSTRACT

The construction and some preliminary measurements of a drift chamber capable of measuring the drift velocity with an accuracy of 0.5% are described. This monitor chamber is connected to and shares a common gas supply with the muon spectrometer of the L3 particle detector at CERN. The monitor chamber is used for correcting the data obtained by the spectrometer. The drift electrons are produced by the photoelectric effect when a UV laser illuminates a gold surface. This system enables us to measure the drift velocity changes due to the change in the parameters of the gas used in the spectrometer.

INTRODUCTION

Elementary particle physicists study the fundamental building blocks of nature by making particles collide and analyzing the debris produced by the collision. One gets information on the particles through their interactions with matter. To 'see' them, however, one needs devices to convert these sub-microscopic interactions into marcoscopically observable signals. A drift chamber is one type of such devices [1].

The pieces of a drift chamber are quite simple.. It is a chamber filled with a special gas mixture. Inside, there are thin sense wire electrodes under positive voltage and a plate electrode or mesh of wires under negative high voltage.

The basic phenomenon underlying the operation of a drift chamber is that a charged particle, passing through the gaseous medium, can ionize the molecules or atoms, leaving ion-electron pairs behind along its track. The electric field present accelerates these free charges. If the electric field is uniform and not too strong, the acceleration by the field and the scattering by the atoms of the medium result in a drift of constant

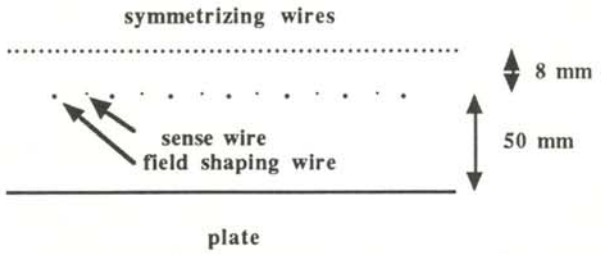

Figure 1
The electrode configuration in the monitor chamber.

Károly is a senior physics student at the Eötvös Lóránd University, Budapest, Hungary. He was a summer exchange student in the High energy Physics group at Union College. He intends to go to graduate school in physics, possibly in the United States.

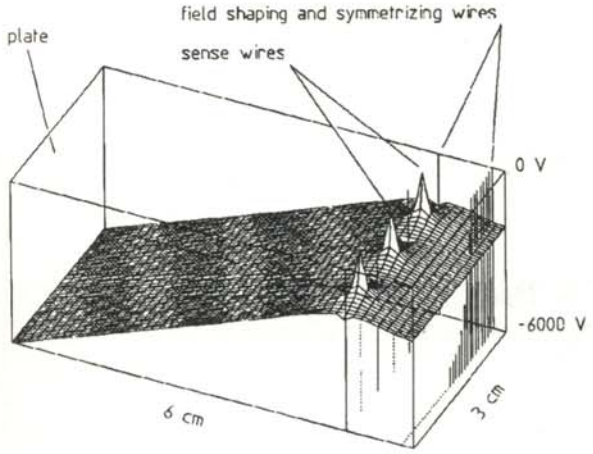

Figure 1
The electrode configuration and the electrostatic potential.

velocity (hence the name 'drift chamber'). The configuration of the drift chamber used in our experiments and the electrostatic potential are shown in Figures 1 and 2. [2]

Figure 3 zooms into Figure 2 and depicts the electrostatic potential around the wires. This picture shows that in the neighborhood of the very thin wires electrodes, the above mentioned conditions for having a drift of constant velocity are not fulfilled. In fact, close to the thin wire, the field is so strong that between two collisions, the electrons can get enough energy to ionize. As a result, the newly liberated electrons accelerate, ionize further and so on... The number of electrons increases rapidly and an avalanche is produced. The avalanche electrons hitting the wire give rise to a current pulse which can be amplified and analyzed.

If the period of time of non-uniform motion close to the wire is negligible in comparison with that of the uniform drift, the distance at which the particle passed the wire by can be calculated:

$$d = v * t \qquad (1)$$

where v is the constant drift velocity and t is the interval between the traversal of the particle through the chamber and the detection of the current pulse.

By reading out several sense wires and/or using a couple of drift chambers, one can determine several points of the path of the particle passing through. One can thereby reconstruct the trajectory of the particle. For accurate position detection, one should know the drift velocity as precisely as possible. The drift velocity, however, depends on parameters of the gas such as pressure, temperature and gas composition. For this reason, it is advisable to monitor the drift velocity changes during trajectory measurements.

ABOUT THE L3 EXPERIMENT

The L3 is one of the four big detectors built at the interaction points of the Large Electron Positron storage ring (LEP) at CERN [3]. Actually, it is a system of numerous detectors of various kinds. For example, a number of drift chambers constitute the muon spectrometer, which measures the momentum of the high energy muons by reconstrucing their trajectory in a known magnetic field.

The precision of the measurement is limited mostly by the intrinsic resolution which is determined by the geometry of the chamber. (For instance, the sense wires cannot be placed arbitrarily close to each other because the electrostatic forces acting between them would distort the alignment.) The error resulting from a 0.5% change in the drift velocity, however, can be of the same order of magnitude as the intrinsic er-

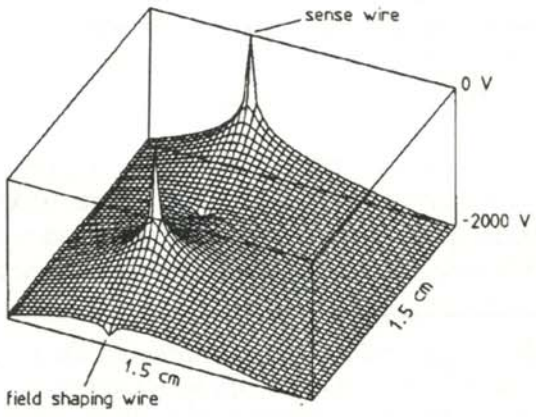

Figure 3
The electrostatic potential in the neighborhood of the wires.

ror of the chamber. That is why it was decided at CERN to monitor the drift velocity change due to the gas parameter changes.

THE MONITOR CHAMBER

Our task was to construct a device which could measure the change of the drift velocity with high precision. We built a small drift chamber. Its electrode configuration is shown in Figure 1. One of the electrodes was a gold plated metallic plane set to -6 kV. The plane of the alternating arrangement of sense and field shaping wires is at a distance of 50 mm from the golden surface. The sense and field shaping wires were 20 and 60 microns in diameter and set to 0 V and -1.9 kV respectively. The spacing between a sense wire and a neighboring field shaping wire was 5 mm. The plane of symmetrizing wires was 8 mm away from the sense and field shaping wires. The symmetrizing wires were 60 microns in diameter set to - 2kV and spaced 1 mm apart. This configuration was similar to that of the main chamber of the spectrometer.

The experimental set-up is sketched in Figure 4. The golden surface was illuminated by UV laser pulses. The laser beam entered the chamber through a quartz window, which, unlike common glass, is transparent to UV light.

From the illuminated spot, the electrons were ejected by the photoelectric effect. They drifted

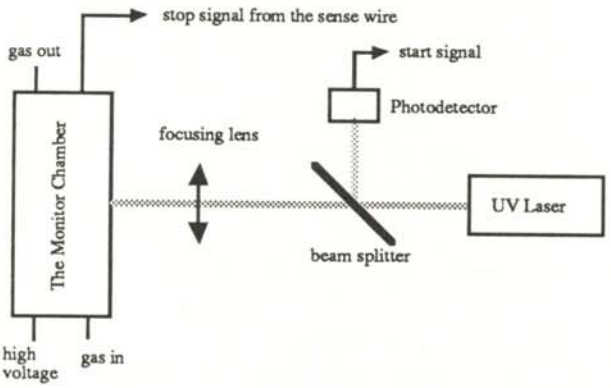

Figure 4
The experimental set-up

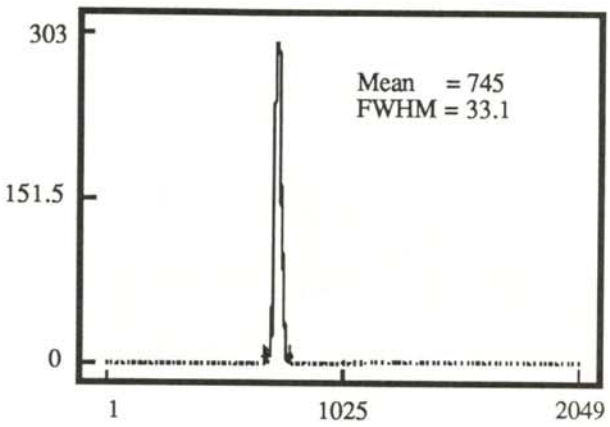

Figure 5
A typical Time-to-digital Converter spectrum. Channel 1 corresponds to a drift time of 1 micro-second.

for about 1 μs until they reached the sense wires. The energy of the UV photons is 3.68 eV while the ionization energy for the gas is about 13-15 eV, so the atoms of the gas do not produce electrons by being ionized by the laser photons.

The UV sensitive photodetector gives a time-to-digital-converter (TDC) the start signal, while the sense wire in front of the illuminated spot gives the stop signal. The TDC is read out by a computer, which collects, processes and displays the data. This experimental set-up makes possible continuous measurements at a rate of 20 pulses per second.

A typical spectrum collected by the TDC is shown in Figure 5. On the horizontal axis, a distance of one channel corresponds to 0.05 ns difference in drift time and the first channel corresponds to 1 μs drift time. This means that we could measure a time interval of about 1 μs with an error of 2 ns. However, the actual accuracy of our measurements are worse, due to the instability of the readout electronics.

To monitor the drift velocity change due to the changes in the gas parameters in the spectrometer, the monitor chamber and the spectrometer have a common gas supply as shown in Figure 6. Preliminary experiments have shown that we

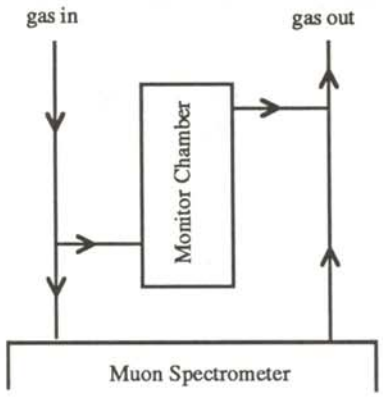

Figure 6
Schematic diagram of the gas system, showing the interconnection between the muon spectrometer and the monitor chamber.

can measure this drift time with an error of 5 ns. This means we have achieved the desired accuracy. We have built two monitor chambers, one of which has been installed at CERN. We are still carrying out experiments with the other one in order to find out how to improve the accuracy of our method.

ACKNOWLEDGMENTS

The author would like to thank L. Baksay, S. Lokos, R. Magahiz (all from Union College, Schenectady, NY, USA) and Gy. L. Bencze, E. Denes, Z. Fodor and P. Koncz (all from the Central Research Institute for Physics, Budapest, Hungary) for making my participation in this project possible and for their support and help.

REFERENCES

*. This paper was presented as a talk at the conference of the International Association of Physics Students, Amsterdam, Netherlands in September 1990.

1. For more information on drift chambers see: R.C. Fernow, Introduction to Experimental Particle Physics, Cambridge University Press, 1986, Chapter 10.

2. The electrostatic potential calculations were done with GARFIELD, a Drift Chamber Simulation Program written by R., Veenhof of CERN

3. For more information on L3, see: Yue Peng, The Muon Spectrometer of the L3 Detector at LAP, CERN booklet.

FACULTY SPONSOR

Professor László Baksay
Physics Department
Union College
Schenectady, NY 12308

(current address)
Department of Physics and Astronomy
The University of Alabama
Tuscaloosa, AL 35487

HEAT TRANSFER INSIDE PLANET EARTH: A NUMERICAL STUDY

William A. Arnold *
Department of Physics
The University of Akron
Akron, OH 44325

ABSTRACT

A simulation was made to address the common conviction that the dominant mode of heat transfer in the non-solid mantle of the earth is convection. The crust, being solid, transfers heat by conduction. The outer core acts like a liquid, but the mode of heat transfer is not explicitly mentioned in the literature. The heat transfer in the inner core is believed to be primarily through conduction. This computer simulation only addresses the heat transfer inside the earth by assuming a conduction limited model. The simulation demonstrates that the earth's crust would be thicker than it is known to be if conduction were the only mode of heat transfer in the mantle.

INTRODUCTION

The earth is known to be segregated into three main layers: the crust; the mantle and the core. The extremely high temperatures encountered beyond a few kilometers depth make physical examination of the earth's interior impossible. Scientists must therefore rely on inferred data from rocks and seismic data to model the interior of the earth. These data can be used as input to numerical simulations to determine the internal workings of our planet. One such set of data are the heat transfer parameters of the materials that make up the earth.

William Arnold graduated from the University of Akron in May 1990 with a BS in physics. He received the NASA Graduate Student Program award and is now attending Clarkson University in Potsdam, NY where he is working on a Ph.D. in Engineering Science.

BACKGROUND DATA ON THE EARTH

The mean temperature at the earth's surface is approximately 280 K (288 K at a 10 meter depth). The temperature at the crust-mantle interface is inferred from the melting point of most rocks, typically in the neighborhood above 1100 K. The best theoretical calculations of the temperature at the outer core-mantle boundary is 4500 K and at the center of the planet as 5000 K. The equatorial diameter is 12,756 km, while the polar diameter is a bit smaller at 12,713 km. The size of the core is fairly well known from seismic readings with the outer core at 7000 km diameter, while the inner core is thought to be 2400 km in diameter [1]. The crust of the earth is 20-70 km thick in continental areas and is made primarily of granitic rocks, while the ocean basin areas are 8 km thick are are primarily basalt in composition.

Volcanic studies of deeply eroded mountain belts indicate that the mantle is composed of ig-

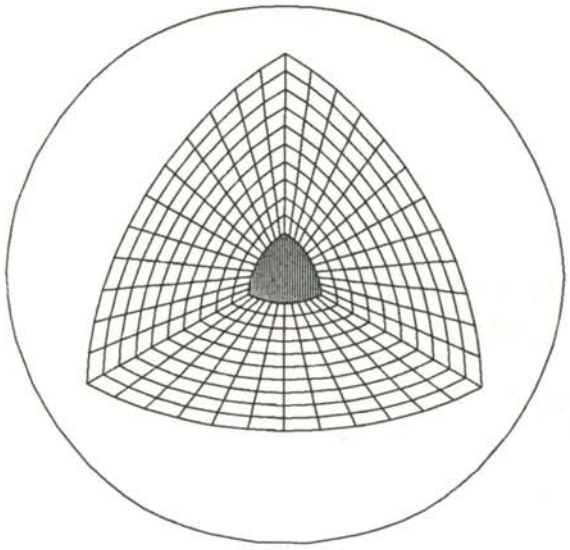

Figure 1
Three dimensional mesh configuration used in the finite element analysis.

neous silicate rocks such as olivine $(Mg_{0.9}Fe_{0.1})_2SiO_4$ [2]. Seismic data indicate the lower mantle contains about 14% FeO [2]. The core is thought to be composed primarily of metallic iron $\{Fe_2O\}$, which is the cosmically most abundant heavy material, to yield an average density of the earth of 5.5×10^3 kg/m^3 (an uncompressed value of 4.5×10^3 kg/m^3).

The gravitational field inside a planet will change with depth. If the earth is assumed to be a perfect sphere instead of an ellipsoid and that it has a core which contains 32.5% of the planet's mass, the gravitational field at the core-mantle boundary would be greater than at the surface. This result must be kept in mind when considering buoyancy effects in convective flows.

THE MODEL

The objective of this study was to show by conduction and energy arguments that a solid earth could not meet the known physical temperature conditions existing in the earth. This solid model does not allow any flow, and hence eliminates convection. This computational work is classified as a conduction limited model.

The earth was modeled as a perfect sphere of radius 12735 km. This approximation is valid since the difference between the polar and equatorial radii is small compared with the size of the finite elements used. The heat flow through the various regions of the earth were modeled using the incompressible continuity equation and those for momentum and energy as well as the equation for heat transfer in a thick hollow sphere. These equations were solved using a finite-element numerical routine. The earth was divided into a three dimensional mesh, as shown in Figure 1. Temperatures at the surface and at the core were used as boundary conditions and the program produced a map of the temperature fields such as the one shown in Figure 2.

The material properties [3,4] used in the model depended on the local temperature. Thus, the conductivity is a temperature dependent parameter. The different layers of the earth were modeled by assigning them the appropriate conductivity and tracking their size via the resulting temperature field.

The set of equations, written in tensor form, describing the complete flow and thermal fields are the incompressible equations of continuity:

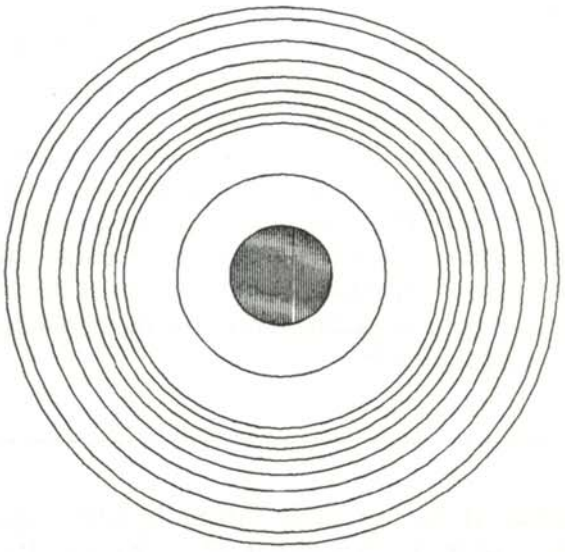

Figure 2
Isotherms of a typical temperature field resulting from the finite element analysis.

$$u_{i,j} = 0, \tag{1}$$

momentum:

$$\rho\,[\partial u_i/\partial t + u_j u_{i,j}] = -\,p_i + \rho f_i + \rho g_i[1 - \beta(T - T_B)] + [\mu(u_{i,j} + u_{j,i})]_j\ , \tag{2}$$

and energy:

$$\rho\, C_p\,[\,\partial T/\partial t + u_i T_{,j}] = (kT_{,j})_{,j} + \mu\phi + q_s\ , \tag{3}$$

where u is veloity, ρ is density, p is pressure, f is the volumetric body force, g is the gravitational field, T is temperature, β is the thermal expansion coefficient, μ is the viscosity, C_p is the specific heat at constant pressure, k is the thermal conductivity, q_s is the volumetric external heat source and ϕ is the viscous dissipation function.

Since we are modeling the earth as a solid, each term in Equations 1-3 containing the velocity vector u is set to zero. In the solid model, both the viscous energy dissipation and the internally applied heat sources are zero. This leaves only:

$$(kT_{,j})_{,j} = \{k\nabla^2 T\} = 0 \tag{4}$$

to be solved. When k, the thermal conductivity, is not a function of temperature, this becomes Laplace's equation. In most cases presented here, however, k is a strong function of temperature and the energy equation becomes a nonlinear equation.

Heat calculations were done using the equation for heat transfer in a thick hollow sphere:

$$Q = -kA(dT/dr) = 4\pi k\,\Delta T\,(r_i r_o)/(r_o - r_i) \tag{5}$$

where A is the area of the boundary, ΔT the temperature difference between the boundaries, r_i and r_o the inside and outside radii, Although the earth is not hollow, this equation is still valid for any two finite radii as long as the temperatures remain constant at the boundaries and the conductivity is constant between the two radii.

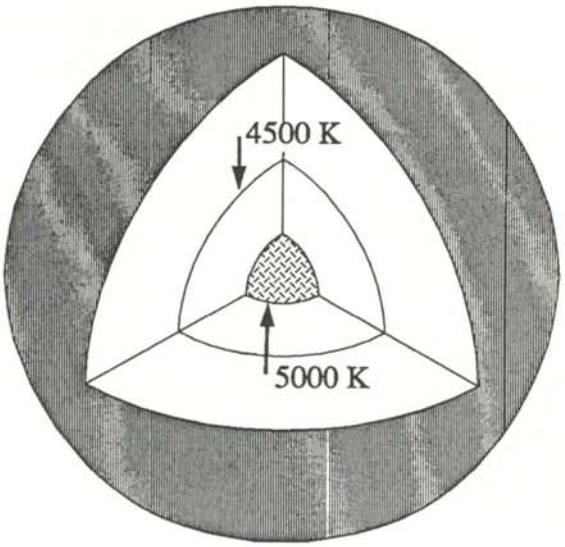

Figure 3
Boundary temperature conditions that are imposed on the inner core.

The equation is valid regardless of the material inside or outside the two radii. Once the two radii of a region of constant conductivity are known, the net heat flux transferred through the surface of the earth can be computed by the use of geometric 'shape factors' [5].

The set of governing equations were then solved using a finite-element based code. [6] Fixed temperature boundary conditions of 280K at the surface of the earth and 5000K at the center were imposed. Because the code used a Cartesian geometry, the 5000K boundary condition has to be placed on a small 'sphere' rather than at a single node at the geometric center of the earth. This is shown in Figure 3.

The material properties used in this model depended upon the local temperature. The crust of the earth, which is composed of basalts and granitic rocks should have a conductivity comparable to that of clay, sandstone, gravel and marble. The upper mantle should have a conductivity comparable to that of igneous silicate rocks. The lower mantle, which is believed to be richer in iron, should have a higher conductivity. Finally, the core should be a conductivity comparable to iron at high temperature and pressure.

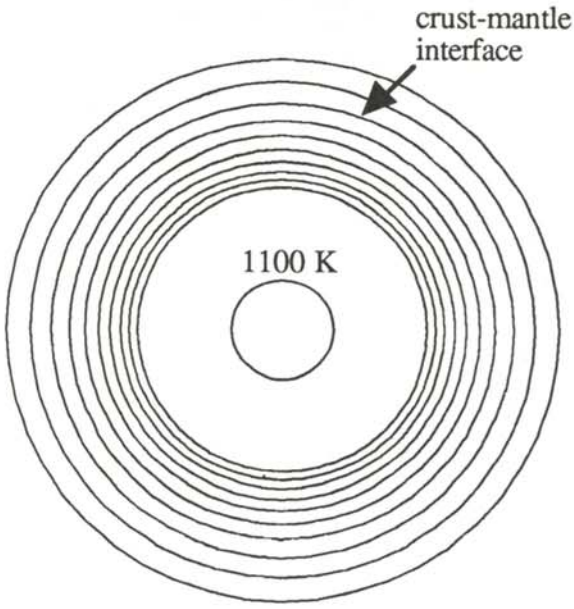

Figure 4
Isotherms for the temperature independent conductivity model. There is a 470 K spacing between the isotherms.

The points of interest of the temperature profile are:
1) 1100K - the crust-mantle interface (the melting point of rocks,
2) 4500 K - the core-mantle interface.
The core size was kept constant by adjusting the boundary conditions inside the core and tracking its size by the 4500K isotherm (see Figure 1). The crust thickness was found by measuring the difference between the surface radius and the radius of the 1100 K isotherm.

RESULTS

Low limit of conductivity
The first test involved the lowest possible limit of the conductivity. The conductivity value of 1.43 W/mK used in the mantle is that of olivine. This ignores the FeO content in the mantle. The outer core diameter was kept at 7 x 10^3 km and at 4500 K. This required that the boundary conditions for the 5000 K sphere inside the core to be adjusted to 2.4 x 10^3 km.

The temperature isotherms, shown in Figure 4, were spherically symmetric. The isotherm spacing was close in the mantle and sparse in the highly conductive core. The location of the 1100 K temperature isotherm, which represents the crust-mantle interface, was measured and found to have a diameter of 11 x 10^3 km. This yields a crust thickness of about 900 km. This is at least an order of magnitude thicker than the actual crust.

If one assumes the actual crust to have an average thickness of about 12 km and a conductivity of basalt, then the actual heat transfer through the crust is on the order of 4 x 10^{13} watts. (This calculated value agrees well with measured experimental values. [7]) Using this model with the outer radius half the diameter of the earth and the crust-mantle interface as the inner radius, the total heat transfer through the crust was calculated to be 5.2 x 10^{11} watts. Thus, the actual heat transferred by the crust is about 80 times the value predicted using the is lower conductivity.

Linear variation of a moderate conductivity
The second test involved having a conductivity of the mantle which varied linearly from 1.43 W/mK at 1200 K to 12 W/mK at 4500K. This

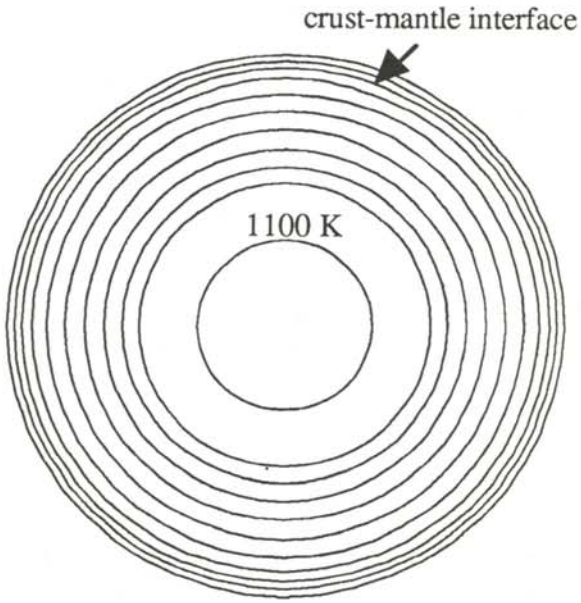

Figure 5
Isotherms for the moderate temperature dependent model. There are 470 K spacing between isotherms.

model of the conductivity takes into account the 14% iron content in the lower mantle. The isotherms, as seen in Figure 5 now are more evenly spaced through the earth. The 1100 K isotherm was found to have a diameter of 12.2 x 10^3 km. This yields a crust thickness of about 270 km. This value is about 20 times the average 13 km thickness of the real crust. The inner boundary condition required that the 5000 K boundary be imposed at the 4100 km diameter. The heat transfer was again computed by the same method and found to be 1.9 x 10^{12} watts, still an order of magnitude lower than the actual value.

Upper limit of conductivity

The final study tested a possible upper limit of the thermal conductivity. The conductivity varied linearly with temperature from 1.43 W/mK at 1200 K to 240W/mK at 4500 K. The upper limit was found by adjusting the upper value of the conductivity until the 1100 K isotherm was at the crust-mantle interface at 12,720 km diameter. This boundary condition produced a conductivity value that is higher than for most materials. The isotherms, shown in Figure 6 are now packed close to the surface of the earth.

To make the finite element analysis work using a three dimensional mesh would have required too much computer time. Therefore, this part of the analysis was performed using an extremely high resolution two dimensional mesh which incorporated an axis-symmetry. The axis-symmetric analysis automatically implied spherically symmetric isotherms. This result is justified with our model, but could not be utilized if convection effects were included.

SUMMARY

The crust thickness predicted by the moderate conductivity limit in this model is an order of magnitude thicker than the actual crust and the predicted total heat transferred by the crust is an order of magnitude lower than the actual value. When the upper value of the conductivity is adjusted to satisfy known crustal boundary conditions, the conductivity is higher than found in most materials. The heat transfer in the earth's mantle therefore cannot be produced by conduction alone. This confirms the common view that heat is transferred by convection in the mantle. The order of magnitude differences in thickness and heat transfer imply that convection is the dominant mode of heat transfer in the mantle.

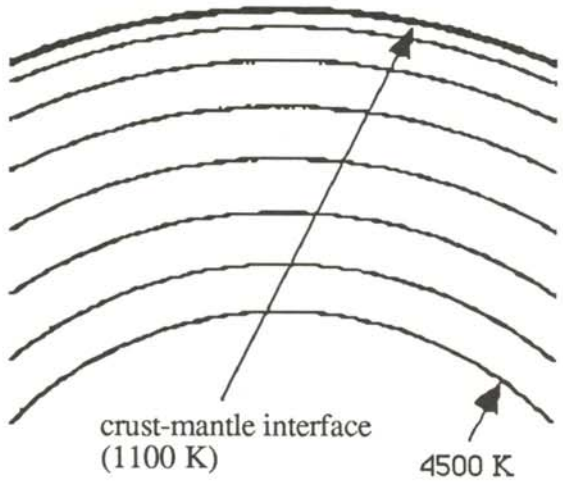

Figure 6
Isotherms for highly temperatue dependent conductivity. Note the change in scale between this figure and Figures 4 and 5. There are 470K spacings between isotherms.

ACKNOWLEDGEMENTS

This model was developed at NASA Lewis Research Center. The author would like to thank Dr. Schneider of the University of Akron for his helpful guidance. He would also like to thank Michele Oziomek and Chuck Panzarella who kindly reviewed the model.

REFERENCES

* present address of author: Department of Electrical and Computer Engineering, Clarkson Hall, Clarkson University, Potsdam, NY 13699-5720

1. Abell, Morrison and Wolf, Exploration of the Universe, CBS College Publishing, 1987.

2. D. L. Anderson, 'Where is the Crust?', Physics Today, March 1989.

3. Eckhert and Drake, Analysis of Heat and

Mass Transfer, McGraw-Hill, 1972.

4. Touloukian, Powell, Ho and Klemens, Thermo-physical Properties of Matter, Plenum Publishing Corp. 1970.

5. J.H. Lienhard, A Heat Transfer Book, Prentice-Hall Inc., 1981.

6. M. Engelman, *FIDAP Theoretical Manual*, Fluid Dynamics International Inc. 1600 Orrington Ave, Evanston, IL 60201, 1987.

7. G.D. Garland, Introduction to Geophysics: Mantle,Core and Crust, W.B.Sanders Co., pp. 340-344.

FACULTY SPONSOR

Dr. Ronald E. Schneider
Department of Physics
Buchtel College of Arts and Sciences
The University of Akron
Akron, OH 44325-4001

A TEST OF CONSISTENCY OF LOW-ENERGY PION-NUCLEON DIFFERENTIAL CROSS SECTIONS WITH PARTIAL CROSS SECTIONS *

Tony S. Hill
Department of Physics
Abilene Christian University
Abilene, TX 79601

ABSTRACT

A chi-squared minimization routine was developed to test the consistency of low-energy pion-nucleon differential cross sections with the results of recent partial cross section measurements. In the analysis, differential cross section measurements made by the University of Colorado-TRIUMF collaboration and partial cross section measurements made by E. Friedman at TRIUMF were used. The result of the test reflects an inconsistency between the two sets of experimental data.

INTRODUCTION

The most fundamental measurement that can be made in πN scattering experiments is the differential cross section. For the πN system specifically, the differential cross section can be defined as the differential target area associated with the nucleon that is perpendicular to the traveling pion's wave vector **k** that yields a deflection of the pion into a differential solid angle. The differential cross section is dependent on the scattering angle, θ, and the wave vector amplitude $|\mathbf{k}|$. The differential cross section can therefore be represented by a Legendre expansion.

$$\frac{d\sigma}{d\Omega} = a_o + a_1 P(\cos\theta) + a_2 P(\cos\theta) + \ldots \quad (1)$$

Tony graduated from Abilene Christian University and is now pursuing a Ph.D. in High Energy Physics at Iowa State University of Science and Technology. He is a research assistant in the DELPHI collaboration (LEP at CERN)

The P_n's are the Legendre polynomials where n is the order of the term. The a_n's are the amplitudes for the polynomials. Each term in the expansion represents specific angular momentum contributions to the differential cross section. The amplitude from each term gives the wave mixing ratio for each momentum state.

The total cross section can then be defined as the target area that yields any deflection of the pion and can be obtained by integrating the differential cross section over all solid angle.

$$\sigma_{total} = \int_\Omega \frac{d\sigma}{d\Omega}\, d\Omega = \int_{-1}^{1} \frac{d\sigma}{d\Omega}\, 2\pi\, d(\cos\theta) \quad (2)$$

A partial cross section is similar to the total cross section except the integration is limited to specified angle limits instead of all angles.

$$\sigma_{partial} = \int_{\theta_{min}}^{\theta_{max}} \frac{d\sigma}{d\Omega}\, 2\pi\, d(\cos\theta) \quad (3)$$

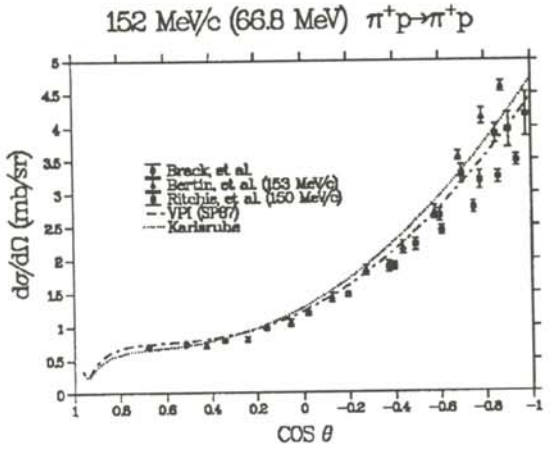

Figure 1
A plot of three generations of differential cross section data. The curves represent two different partial wave solutions. Note the discrepancies at increasing back angles.

Elementary scattering theory [2] allows one to represent the scattering process by wave functions that are characterized by parameters called phase shifts. Phase shifts are simply the shift in phase of the wave function at large distances from a scattering potential as a result of the interaction with that potential. There will be phase shifts for each state of angular momentum available to the system. Partial wave solutions obtain the phase shifts for a reaction by incorporating dynamical and internal symmetries along with the current body of data for a particular reaction. The partial wave solutions also incorporate Coulomb contributions in their measurement predictions.

Figure 1 is a comparison plot of some differential cross section data and two partial wave solutions. The minima that occur in the two partial wave solutions in Figure 1 at cos θ = 0.9 are due to destructive interference between the hadronic and coulomb scattering amplitudes. The sharp rise in the solutions as the angle approaches zero is characteristic of the Coulomb dependence in the Rutherford cross section

$$\sigma = (\sin^4(\theta/2))^{-1}. \qquad (4)$$

The question of consistency in the body of low-energy pion-nucleon (πN) scattering data has recently been introduced by theorists working with chiral perturbation theory [1]. The relationship between πN scattering amplitudes and quark content of the hadrons within the framework of chiral perturbation theory is demonstrated in Figure 2 (adapted from Reference 1). The shaded area is the region of physical measurements.

Due to their analytic behavior, scattering amplitudes can be extrapolated into the non-physical region to the Cheng-Dashen point to extract the πN sigma (σ) term that yields quark flavor relationships for the hadrons. For any extrapolation of these amplitudes to be meaningful, the body of πN scattering data from which they are determined must be consistent.

There is some ambiguity in comparing experimental results with the partial wave solution [2]. A plot of some of the data available for the reaction near 150 MeV/c is displayed in Figure 1. These differential cross sections are some of the lowest energy data available for πN elastic scattering. The three sets of experimental data represent three generations of experiments: the Saclay data [3] are 15 years old, the University of Maryland-LAMPF [4] are eight years old, and the University of Colorado-TRIUMF [5] are the most recent. Note the discrepancies at the back angles. These discrepancies lead to ambiguities in

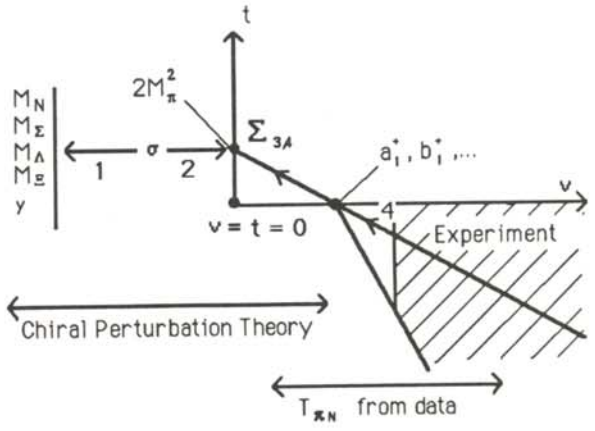

Figure 2
Schematic representation of the extrapolation made in chiral perturbation theory from analytic functions derived from experimental data to the quark content of the hadrons. Adapted from Reference 1

the entire body of data. The Karlsruhe [6] and VPI(SP87) [7] partial wave solutions (shown in Figure 2) rely on analytic continuations of the body of data. In particular, the Colorado-TRIUMF data are claimed to be inconsistent with the analyticity constraints used in that analysis. [8]

DATA SELECTION

Data for partial cross sections have recently been obtained at TRIUMF. A sketch of the experimental arrangement used [9] to measure partial cross sections for π+p -> π+p at 66.8 MeV is shown in Figure 3. In this experiment anti-coincidence was employed; that is, whenever a particle detected by the beam counter did not scatter into the scintillation detector, it was recorded as an event. This experimental arrangement effectively measured the partial cross section, in this case from 20° to 180° and from 30° to 180°, by simple geometric placement of the detector. It is these data that will allow an unambiguous comparison of the differential cross section data with the partial wave solutions. The results presented for the partial cross sections are:

$$\sigma_{partial} = 20.8 + 0.5 \text{ mb}; \quad 30° \le \theta_{cm} \le 180°$$

$$\sigma_{partial} = 21.8 + 0.5 \text{ mb}; \quad 20° \le \theta_{cm} \le 180°$$

These data are consistent with the low-energy partial wave solutions.

The differential cross sections chosen for the test against the partial cross section results are the University of Colorado-TRIUMF acquisitions. There are three reasons for this selection: the relatively complete angular distribution of differential cross section data allows for a comparison via integration with partial cross section results, the data have the lowest quoted errors (see Figure 1), and they are the most recent. The data were acquired in three different beam channels with three different beam normalizations yet they are consistent in areas where angular measurements overlap.

To fit the Colorado -TRIUMF data so that the comparison can be made with the partial cross sections, a Legendre expansion was utilized (as in Equation 1). Due to the short range of the hadronic force and the low pion beam energy, scattering occurs only in S and P wave states which correspond to a second order expansion.

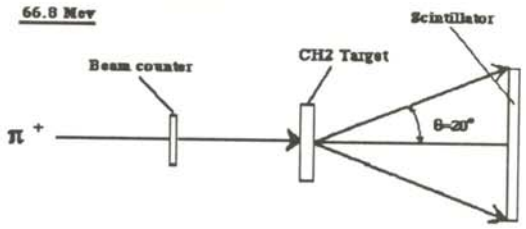

Figure 3
Simplified diagram of Friedman's anti-coincidence experiment conducted at TRIUMF

$$\frac{d\sigma}{d\Omega} = a_o + a_1 P(\cos\theta) + a_2 P(\cos\theta) \qquad (5)$$

For a direct comparison of the Colorado - TRIUMF data to Friedman's results, the integration of the Colorado -TRIUMF differential cross section is limited to the angles used in the partial cross section experiment, in this case from 20° to 180°.

$$\sigma_{partial} = \int_{\cos 20°}^{\cos 180°} \frac{d\sigma_{fit}}{d\Omega} 2\pi \, d(\cos\theta) \qquad (6)$$

FITTING PROCEDURE

The program used to fit the data was a reduced chi-square minimization routine[10]. A chi-square fit to the data is defined as:

$$\chi^2 = \sum_{i=1}^{N} \frac{\left\{ \frac{d\sigma_{exp}}{d\Omega} - \frac{d\sigma_{fit}}{d\Omega} \right\}^2}{\delta^2 \left\{ \frac{d\sigma_{exp}}{d\Omega} \right\}} \qquad (7)$$

The reduced chi-square is then:

$$\chi^2_{reduced} = \frac{\chi^2}{N - (n+1)} \quad (8)$$

where N is the number of data and the (n+1) term is the number of fit parameters (n is the order of Legendre expansion).

In the test developed, further constraints are placed on the fitting routine by adding a term in the reduced chi-square equation that allows for a dependence on the difference between experimental (Friedman) and calculated (from the fit to the Colorado -TRIUMF) partial cross sections.

$$\chi^2_{reduced} = \frac{W\,\{\sigma^{exp}_{partial} - \sigma^{fit}_{partial})^2}{\delta^2(\sigma^{exp}_{partial})} + \sum_{i=1}^{N}\left[\frac{\left\{\frac{d\sigma_{exp}}{d\Omega} - \frac{d\sigma_{fit}}{d\Omega}\right\}^2}{\delta^2\left\{\frac{d\sigma_{exp}}{d\Omega}\right\}}\right]}{N + W - (n+1)} \quad (9)$$

where W is a weighting factor that is used to weight each experiment against the other. For instance, if W = 1 the contribution of the partial cross section difference is that of a single differential cross section point or, if W = 16, the two experiments are weighted equally, since there are 16 data points for $d\sigma/d\Omega$.

Figure 4 is a comparison plot of three different fits generated by the modified reduced chi-square routine from different initial conditions. Fit I is a simple fit to the differential cross section data with no partial cross section considerations (W = 0, n = 2). Fit II represents equal consideration for both experiments (W = 16, n = 2). Fit III is also one in which the experiments are equally weighted but also has higher degrees of freedom in the Legendre expansion (W = 16, n = 7).

Fit I has no partial cross section constraints, and therefore is just a simple best fit to the differential cross section data. The calculated partial cross section from this fit is 18.7 mb, which is smaller by six standard deviations than Friedman's measurement of 21.8 mb. The reduced chi square for this fit is 0.45.

In Fit II, the two experiments are weighted equally (W = 16). It is obvious that the routine is performing as desired by the way it basically splits the data fit (W = 0) and the partial cross section constraint. The partial cross section is increased to a median value of 20.2 mb at the expense of a simple fit through the differential cross sections. The reduced chi-square for the fit is 11.3.

In Fit III, the experiments are again weighted equally. This fit, however, has more degrees of freedom (n = 7) for the expansion. The partial cross section constraint is met; the fit through the differential cross sections is also met. The higher order terms in the Legendre expansion allowed the routine to compensate in the shallow angle area for the partial cross section where it is unconstrained by data. The seventh order fit, though physically meaningless, is the best indication that the routine is behaving properly under what can be considered extreme conditions. The π+p -> π+p reaction at 152 MeV/c is characterized strictly by S and P angular momentum states (n = 1 and n = 2, respectively).

The rise in the plot at shallow angles starting at about $\cos\theta = 0.7$ should not be interpreted as a fit to the Coulomb potential -- there are no Coulomb considerations in the fitting routine. Shallow angle measurements exist for slightly lower energies and are consistent with the partial wave solutions. The minima for the destructive interference between the hadronic and Coulomb potential occur near $\cos\theta = 0.9$ at 55 MeV. So a seventh order fit is not inferring higher order contributions in the 66.8 MeV system but reflects the success of the fitting routine in meeting the imposed partial cross section constraints.

SUMMARY

The simple fit to the Colorado -TRIUMF differential cross section data (Fit I) reveals the inconsistency between the experimental results and the partial wave solutions at a basic level. Adding contributions to the chi-square minimization routine to allow equal weighting of exper-

imental differential cross section data and predicted partial cross sections (Fit II) was not enough to force a second order Legendre expansion to a reasonable calculated partial cross section. The only way that the contributions from both terms in the reduced chi-square could be minimized was to allow for higher order terms in the Legendre expansion to compensate for the partial cross section constraint (Fit III) in the shallow angle areas where the fit was unconstrained by differential cross section data. A seventh order fit, though, is physically meaningless. Therefore, the differential cross section data and the partial cross section data are mutually inconsistent.

ACKNOWLEDGEMENTS

The author would like to thank Dr. Michael Sadler for the opportunity to participate in Abilene Christian University's pion-nucleon research effort and for his guidance throughout my involvement.

REFERENCES

* Current address of author:
Department of Physics, 12 Physics Building,
Iowa State University, Ames, IA 50011.

1. J. Gasser, Second International Workshop on πN Physics, Los Alamos, NM, LA-11184-C.

2. R.J. Cence, Pion-Nucleon Scattering, Princeton University Press, New Jersey, 1969.

3. P.Y. Bertin *et. al.*, Nucl. Phys. B106, 341 (1976).

4. B.G. Ritchie et al., Phys. Lett. 125B, 128 (1983).

5. J.T. Brack et al., Physical Review C 40-6, 2780(1989).

6. R. Koch and E. Pietarinen, Nucl. Phys. A336, 331(1980).

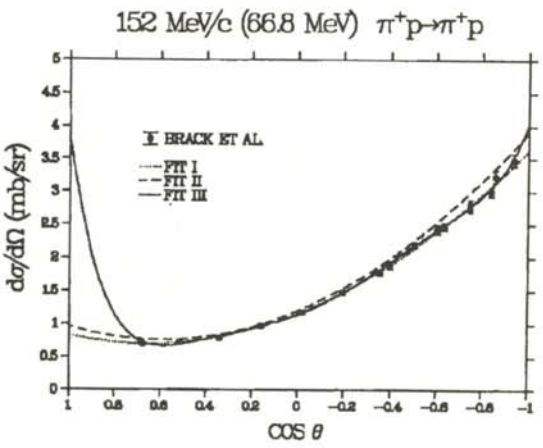

Figure 4
A plot of the University of Colorado - TRIUMF data and three different chi-squared fits. Fit I is a simple fit with no partial cross section considerations. Fit II represents equal consideration for both experiments. Fit III is one in which the experiments are equally weighted, but more degrees of freedom in the Legrendre expansion are included.

7. R.A. Arndt *et. al.*, Phys. Rev. D32, 1085 (1985).

8. G. Höhler, TRIUMF πN Workshop, Vancouver, British Columbia, July, 1989.

9. E. Friedman, πN Newsletter 2, 31(1990), G. Höhler, W. Kluge, and B.M.K. Nefkens, editors. In the U.S., copies may be obtained from B.M.K. Nefkens, UCLA, Los Angeles, CA 90024.

10. The original program was developed by Glenn Olah, a former ACU student.

FACULTY SPONSOR

Dr. Michael E. Sadler
Physics Department
Abilene Christian University
Box 7646
Abilene, TX 79699

The Journal of Undergraduate Research in Physics

The **Journal of Undergraduate Research in Physics** is the journal of Sigma Pi Sigma and the Society of Physics Students. It is published by the Physics Department of Guilford College, Greensboro NC. Inquiries about the journal should be sent to the editorial office.

The Journal of Undergraduate Research in Physics

Editorial Office -

Physics Department
Guilford College
Greensboro, NC 27410
919-292-5511 (voice)
919-854-3606 (FAX)

Editor -

Dr. Rexford E. Adelberger
Professor of Physics
Department of Physics
Guilford College
Greensboro, NC 27410

The Society of Physics Students

National Office -

Dr. Donald Kirwin, Executive Director
Dr. Edwin Goldin, Associate Director
Society of Physics Students
American Institute of Physics
1825 Connecticut Avenue, N.W.
Suite 213
Washington, DC 20009
202-232-6688

President of the Soceity -

Dr. Gary Agin
Department of Physics
Michigan Technological University

President of Sigma Pi Sigma -

Dr Reuben James
Department of Physics
SUNY College at Oneonta